Schweizerischer Erdbebendienst
Service Sismologique Suisse
Servizio Sismico Svizzero
Servizi da Terratrembels Svizzer

Eidgenössische Technische Hochschule Zürich
Swiss Federal Institute of Technology Zurich

Lucerne - Werkhofstrasse (SLUW)

SITE CHARACTERIZATION REPORT

Valerio POGGI, Clotaire MICHEL, Daniel ROTEN

Jan BURJANEK, Carlo CAUZZI, Donat FÄH

Sonneggstrasse 5 CH-8092 Zürich Switzerland; E-mail: clotaire.michel@sed.ethz.ch

Last modified : November 5, 2013

Abstract

Ambient vibration array measurements were performed to characterize the site Lucerne Werkhofstrasse. The site, where the new station SLUW of the Swiss Strong Motion Network was installed, is located in the centre of the deep sedimentary basin of Lucerne. In order to characterize the velocity profile under the station, passive array measurements, active MASW experiment and downhole seismics were performed. The measurements allowed deriving a velocity model for this site. The soil column underlying station SLUW consists in a low-velocity part with a small velocity inversion in the first 10 meters, followed by a progressive increase below this depth, from about 300 to 1000m/s. The larger velocity contrast is found at about 200m (the bedrock interface). The bedrock velocity appears to be realistic (around 1800m/s), but should be confirmed from independent analysis. A 3D behaviour of the sedimentary basin has been shown with a fundamental resonance peak at $1.15\,\mathrm{Hz}$. $V_{s,30}$ is $214\,\mathrm{m/s}$, which would correspond to ground type C in the Eurocode 8 [CEN, 2004] and D for the SIA261 [SIA, 2003]. The theoretical 1D SH transfer function and impedance contrast of the quarter-wavelength velocity computed from the inverted profiles show large amplifications at the resonance frequencies. Recordings on the new station will allow to compare to these simple models.

Contents

1 Introduction **4**

2 Experiment description **5**

2.1 Ambient Vibration sources 5

2.2 Active seismic sources 5

2.3 Equipment 5

2.4 Geometry of the arrays 6

2.5 Positioning of the stations 8

3 Data quality **11**

3.1 Usable data 11

3.2 Data processing 11

4 H/V processing of the passive experiment **13**

4.1 Processing method and parameters 13

4.2 Results 13

4.3 Polarization analysis 16

5 Processing **17**

5.1 Processing methods and parameters for the passive data 17

5.2 Processing methods and parameters of the active data 17

5.3 Obtained dispersion curves from the passive analysis 17

5.4 Obtained dispersion curves from the active analysis and merging with the passive results 21

6 Results of the downhole experiment **25**

7 Inversion and interpretation **27**

7.1 Inversion 27

7.2 Interpretation 27

7.3 Travel time average velocities and ground type 31

7.4 SH transfer function and quarter-wavelength velocity 31

8 Conclusions **34**

References **36**

1 Introduction

The station SLUW (Luzern Werhofstrasse) is part of the Swiss Strong Motion Network (SSMNet) in Lucerne. It was installed in 2011 in the frame of the SSMNet Renewal project. This project includes also the site characterization. Passive array measurements have been selected as a standard tool to investigate these sites. In some cases like Lucerne, it is complemented by an active seismic (MASW) experiment and a CPT (Cone Penetration Test) measurement campaign (level 2 of site characterization).

A passive measurement campaign has been already performed in Lucerne train station in 2007 [Poggi et al., 2012c] and provided the whole velocity profile down to the bedrock. Moreover, an extensive single station measurement campaign was performed between 2006 and 2007 resulting in the mapping of the bedrock depth under the basin of Lucerne [Poggi et al., 2012c]. To improve the characterization at the station site, a small aperture array was additionally performed the night between the 21st and the 22nd March 2011, exactly at the station site (Fig. 1), in order to characterize the upper layers under the station. Moreover, in date 14.04.2011 an active seismic experiment has been performed at this site, with the aim of mapping the phase velocity dispersion function of the surface-waves at high-frequency (>10Hz), in order to extend the resolution of the passive seismic surveys on the shallower part of the velocity model. Finally, a CPT measurement campaign was performed by a private company (Geoprofile subcontracting the company geotechnik.com) on December 13th 2012. At the same time, downhole seismics was also performed. This report only presents the results related to the linear parameters of the ground (especially the shear wave velocity), a separate report is presenting the non-linear aspects and the CPT measurement. This report details the seismic measurement setups, the results of the H/V analysis, especially the fundamental frequencies and of the processing of the surface waves (dispersion curves). Then, an inversion of these results into velocities in the different identified layers is performed, combining all experiments. Finally, several parameters are derived to predict site amplification.

Canton	City	Location	Station code	Site type	Slope
Luzern	Luzern	Werkhofstrasse	SLUW	Lacustrine basin	Flat

Table 1: Main characteristics of the study-site.

Figure 1: Picture of the site.

2 Experiment description

2.1 Ambient Vibration sources

The ground surface is permanently subjected to ambient vibrations due to:

- natural sources (ocean and large-scale atmospheric phenomena) below $1\,\mathrm{Hz}$,
- local meteorological conditions (wind and rain) at frequencies around $1\,\mathrm{Hz}$,
- human activities (industrial machines, traffic…) at frequencies above $1\,\mathrm{Hz}$ [Bonnefoy-Claudet et al., 2006].

The objective of the measurements is to record these ambient vibrations and to use their propagation properties to infer the underground structure. First, the polarization of the recorded waves (H/V ratio) is used to derive the resonance frequencies of the soil column. Second, the arrival time delays at many different stations are used to derive the velocity of surface waves at different frequencies (dispersion).

2.2 Active seismic sources

For the active experiment, a special device was use as active source, consisting of a mass of $120\,\mathrm{kg}$, dropped from a height of up to $2\,\mathrm{m}$ (see Fig. 2). Two shot-offset distances were tested (8 and $20\,\mathrm{m}$) because the distance at which the surface-waves start developing from the source is generally unknown (without some prior knowledge on the local velocity structure). Ten consecutive wave-field excitations have been performed for each source off-set, with the goal of improving the signal-to-noise ratio by stacking in the time (classical f-k method, CIT.) or in the frequency (wavelet t-f-k method, [Poggi et al., 2012a]) domain.

Moreover, for the downhole seismic survey, a classical hammer was used on a metal plate (Fig. 3). The offset was constant, approximately equal to $2\,\mathrm{m}$, even though this information is not provided by the company. Timing information was supplied by a trigger attached to the hammer. In an effort to increase the amplitude of SH waves induced by the hammer, the metal slab was positioned roughly vertically against the wall of a $\sim 30\,\mathrm{cm}$ deep excavation, facing the borehole.

2.3 Equipment

For the passive measurements 12 Quanterra Q330 dataloggers named NR01 to NR12 and 14 Lennartz 3C 5 s seismometers were available (see Tab. 2). Each datalogger can record on 2 ports A (channels EH1, EH2, EH3 for Z, N, E directions) and B (channels EH4, EH5, EH6 for Z, N, E directions). The time synchronization was ensured by GPS. The sensors are placed on a metal tripod in a $20\,\mathrm{cm}$ hole, when possible, for a better coupling with the ground.

For the active measurements, two types of instrumentation were used together (Fig. 4); an array of 24 vertical geophones (10Hz corner frequency, GEODE system), with 1m distance

Figure 2: The 120kg dropping mass device which has been used as artificial source to stimulate the generation of Rayleigh waves.

between, and an array of 7 two-channel seismological stations (same as for the passive measurements), with 2m inter-distance. Combining these two equipments theoretically allows having the large spatial resolution (from the dense geophone array) together with the possibility of using three component recordings.

For the downhole seismic survey, a 3C geophone built in the penetrometer (Type S15CFII15) was used. Acquisition was made through a laptop together with the other channels of the penetrometer.

Experiment	**Digitizer**	**Model**	**Number**	**Resolution**
Passive		Quanterra Q330	12	24 bits
Active		Geode	1	24 bits
Active		Quanterra Q330	7	24 bits
Downhole		?	1	? bits
Experiment	**Sensor type**	**Model**	**Number**	**Cut-off frequency**
Passive	Seismometer	Lennartz 3C	14	0.2 Hz
Active	1C Geophone	?	24	10 Hz
Active	Seismometer	Lennartz 3C	14	0.2 Hz
Downhole	Geophone	?	1	? Hz

Table 2: Equipment used.

2.4 Geometry of the arrays

The array configuration (passive measurement) include 3 rings of 10, 20 and 30 m radius with 3, 5 and 5 sensors, respectively, around a central station, i. e. with a total of 14 sensors. The

Figure 3: Hammering during the downhole seismic test.

Figure 4: The surface-wave survey line. In the picture, only the 14 high-resolution three-component seismological stations are visible, while the geophone string of 24 elements is hidden in the grass.

aperture is therefore $60\,\mathrm{m}$. The experimental setup is displayed in Fig. 5. The final usable datasets are detailed in section 3.2.

For the active seismic measurements, 2 parallel seismic lines of 24 geophones and 14 seismometers were installed, with a spacing of respectively 1 and $2\,\mathrm{m}$, i.e. with a length of 23 and $26\,\mathrm{m}$, respectively (Fig. 6)

For the downhole measurement, the penetrometer was pushed vertically into the ground, approximately $3\,\mathrm{m}$ away from the SSMNet station SLUW. The downhole experiment was performed from 1 down to $31\,\mathrm{m}$ depth.

2.5 Positioning of the stations

The sensor coordinates of the passive measurement were measured using a differential GPS device (Leica Viva), including only a rover station. The differential GPS computation is done on the fly using a GSM link with Swisstopo. It allows positioning with a theoretical accuracy of about $3\,\mathrm{cm}$ on the Swissgrid. However, the quality of the GPS data was low and all points could not be obtained with the required precision (Fig. 5).

A first GPS measurement was performed just after installing the stations (21.03.2011). Only points LUW103, LUW201, LUW205 and LUW303 were positioned with the required accuracy of $5\,\mathrm{cm}$. The other points were positioned with an accuracy of 1 to $2.6\,\mathrm{m}$. Raw data were not recorded so that no post-processing was possible.

Therefore, a second GPS measurement was performed on 21.03.2011 in order to increase the positioning accuracy by recording the raw data. Finding the sensor placement was not always accurate depending on the traces left. 5 more points were positioned with the required accuracy: LUW000, LUW101, LUW203, LUW302, LUW305. The additional error due to the unknown exact sensor placement is low in these cases because of the presence of holes dug to place the

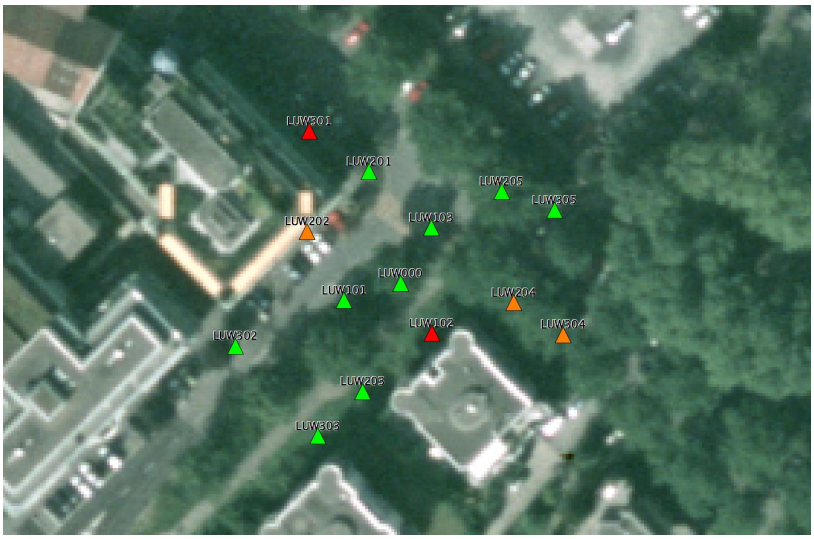

Figure 5: Geometry of the passive array measurement. Color is related to the positioning accuracy obtained on the field after the second measurement. Green: lower than $5\,\mathrm{cm}$, Orange: between 1 and $1.5\,\mathrm{m}$. Red: greater than $1.5\,\mathrm{m}$.

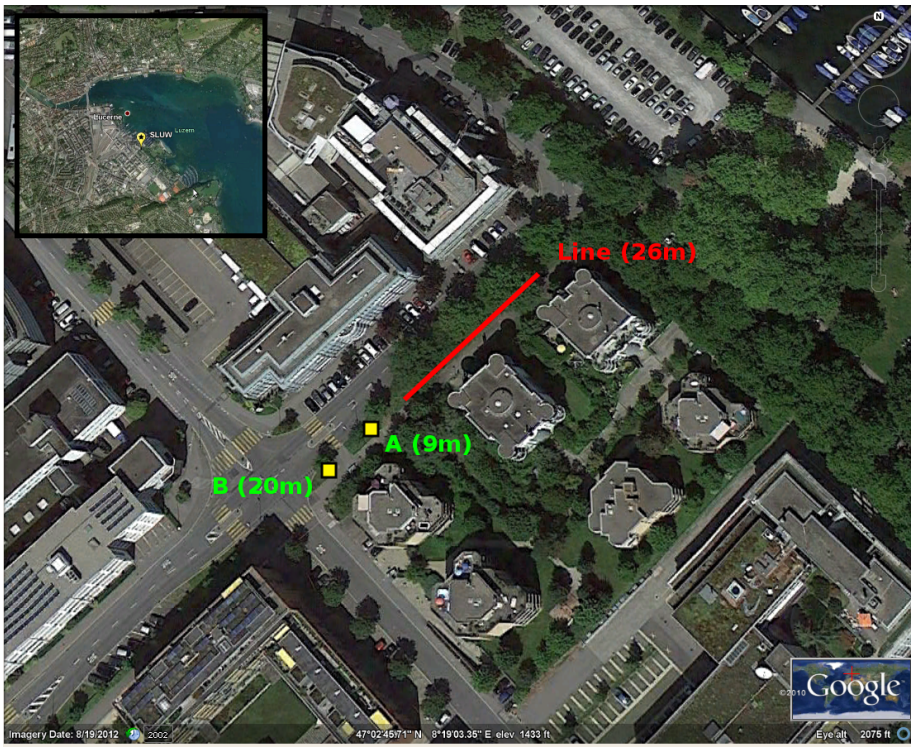

Figure 6: Location of the seismic line (in red) and the two wave-filed excitations (A at 9m and B at 20m) with yellow squares.

sensors and of pictures of the experiment. The accuracy of other points except LUW301 could be improved but still remaining in the order of 1 to $2\,\mathrm{m}$. Moreover, the placement of points LUW102 and LUW202 was quiet clear during the second measurement and is realistic on the Swissimage, whereas the placement of LUW204, LUW301 and LUW304 had no possibility to be improved (on the walkway).

In order to reprocess the raw data of the second measurement to improve the accuracy especially of points LUW102 and LUW202, GPS data of a virtual reference close to the array with $1\,\mathrm{Hz}$ sampling rate at the time of the 2$^{\mathrm{nd}}$ GPS measurement were downloaded from the AGNES web server of Swisstopo (http://www3.swisstopo.ch/). The differential computation was then performed using the Leica Geo software. After this processing, points LUW102, LUW202, LUW204 and LUW304 were obtained with a better accuracy (20 to $40\,\mathrm{cm}$), although some doubt remains on this positioning.

The influence of the poor accuracy of some of the points will be tested in the array analysis.

The relative positioning of the sensors for the active experiment was performed using a measuring tape, with an accuracy of $10\,\mathrm{cm}$. The absolute positioning of the seismic line was performed on the Swissimage, with an accuracy of $2\,\mathrm{m}$.

The relative placement of the active seismic experiment was done using measuring tape and the absolute placement using the aerial photographs.

3 Data quality

3.1 Usable data

The largest time windows were extracted from the passive measurement, for which all the sensors of the array were in position and the GPS synchronization was ensured. One can extract a datasets either in maximizing the recording duration and or in optimizing the quality, removing forty minutes during which GPS measurements were performed close to the sensors. This second option was used in the following. The characteristics of this dataset are detailed in Tab. 3. The surroundings were quiet during the recording, especially because the police closed the road close to point LUW302. Few cars went through the array during the measurement.

For the active experiment, for the each wave-field excitation, a recording of about 2s was performed when using the GEODE data-logger. These consecutive recordings have been then merged in a unique continuous stream of data, removing the noisy tail of the traces (Fig. 7). Conversely, the seismological stations recorded continuously, so that a manual selection of the usable part of the recording had to be performed. It has to be noticed that not all the shots were identically successful during the experiment. Therefore, a further selection on the quality of the performed wave-field excitation has been performed. As such, only the best shots were selected and gathered into a continuous stream.

For the downhole experiment, recordings of each shot, each meter in depth, are available from 1 down to $31\,\mathrm{m}$ depth. Because of the compressor supplying the penetrometer and a small generator providing power to the equipment of the company, the noise level was generally high (Fig. 3). Several geophone traces were stacked to improve the signal-to-noise ratio, but no clear signal for the S-wave arrival could be obtained at depths exceeding 31 m. Due to interferences between P, S- and Rayleigh-waves near the surface the profiling is only considered reliable at depths of more than 5 meters according to the company.

3.2 Data processing

The data were first converted to SAC format including in the header the coordinates of the point (CH1903 system), the recording component and a name related to the position. The name is made of 3 letters characterizing the location (LUW here for the passive and LU1 for the active). For the active line, numbers are increasing from 01 to 14, 1 digit for the ring and 2 more digits for the number in the ring. The response of the sensor was not corrected and the values (in counts) were not converted to $\mathrm{m/s}$.

Dataset	**Starting Date**	**Time**	**Length**	F_s	**Min. radius**	**Aperture**	**# of points**
1	2011/03/21	22:56	182 min	200 Hz	10 m	60 m	14
active	2011/04/14	09:49	104 min	200 Hz	2 m	26 m	14

Table 3: Usable datasets.

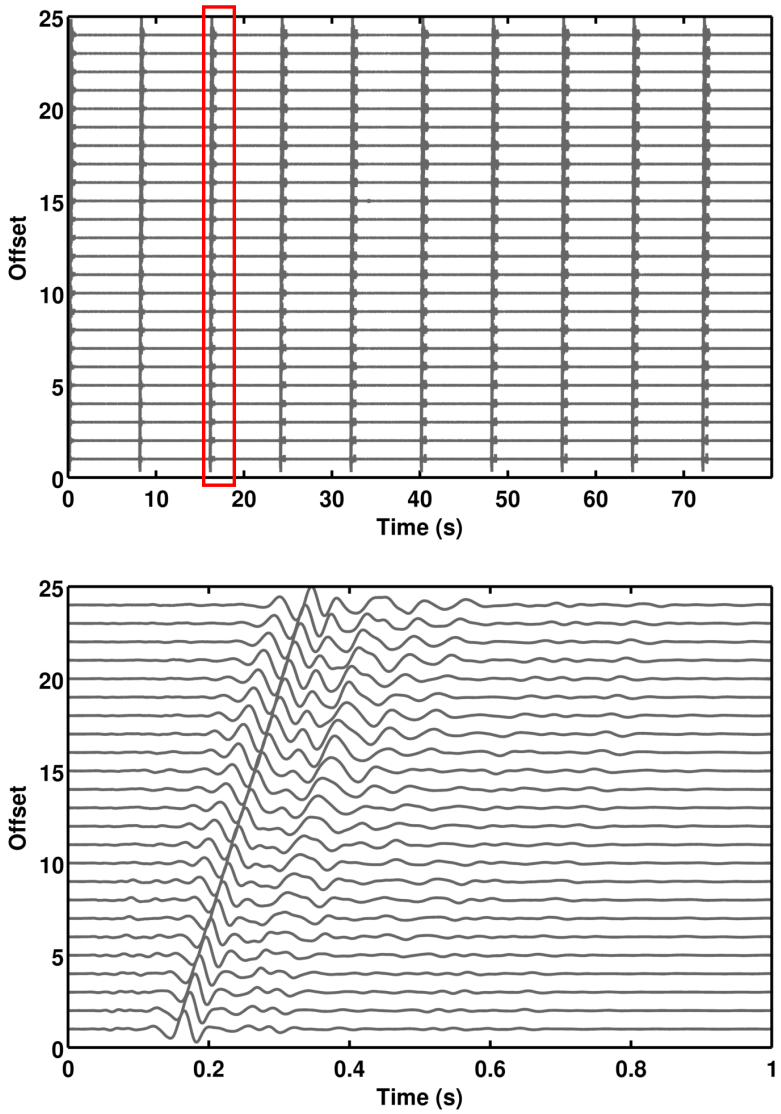

Figure 7: Top: an example of ten consecutive wave-field excitations using the 120kg dropping mass recorded from the geophone line. Bottom: a detail of the one single shot of the same line.

4 H/V processing of the passive experiment

4.1 Processing method and parameters

In order to process the H/V spectral ratios from the passive measurements, several codes and methods were used. The classical H/V method was computed using the Geopsy `http://www.geopsy.org` software. It averages the ratio of the smoothed Fourier Transform of selected time windows. Tukey windows (cosine taper of 5% width) of $50\,\mathrm{s}$ long overlapping by 50% were selected. The smoothing was done using the Konno and Ohmachi [1998] procedure with a b value of 80. The classical method computed using the method of Fäh et al. [2001] was also performed

Moreover, the time-frequency analysis method [Fäh et al., 2009] was used to estimate the ellipticity function more accurately using the Matlab code of V. Poggi. In this method, the time-frequency analysis using the Wavelet transform is computed for each component. For each frequency, the maxima in time (10 per minute with at least $0.1\,\mathrm{s}$ between each) in the TFA are determined. The Horizontal to Vertical ratio of amplitudes for each maxima is then computed and statistical properties for each frequency are derived. The used wavelet is a Cosine wavelet with parameter 9. The mean of the distribution for each frequency is kept. For the sake of comparison, the time-frequency analysis by Fäh et al. [2001], based on the spectrogram, was also used, as well as the wavelet-based TFA coded in Geopsy.

Method	Freq. band	Win. length	Anti-trig.	Overlap	Smoothing
Standard H/V Geopsy	$0.2 - 20\,\mathrm{Hz}$	$50\,\mathrm{s}$	No	50%	K&O 80
Standard H/V D. Fäh	$0.2 - 20\,\mathrm{Hz}$	$30\,\mathrm{s}$	No	75%	?
H/V TFA Geopsy	$0.2 - 20\,\mathrm{Hz}$	Morlet m=8 fi=1	No	-	?
H/V TFA D. Fäh	$0.2 - 20\,\mathrm{Hz}$	Specgram	No	-	?
H/V TFA V. Poggi	$0.2 - 20\,\mathrm{Hz}$	Cosine wpar=9	No	-	No

Table 4: Methods and parameters used for the H/V processing.

4.2 Results

The results show a homogeneous region regarding the H/V ratios. The peak is well defined between 1.23 and $1.26\,\mathrm{Hz}$ (Fig. 8). The shape of the ratios for points LUW202 and LUW303 is slightly different, which is difficult to explain. Using the Time-Frequency analysis does not change much the picture (Fig. 8 bottom). The comparison of all available methods is displayed on point LUW000 (Fig. 9), in which the classical methods were arbitrary divided by $\sqrt{2}$. The matching above the resonance frequency is almost perfect except smoothing issues. The TFA code of V. Poggi shifts the resonance frequency peaks. This could be due to the removal of the SH contribution. It leads to lower frequency values for the ellipticity peak (between 1.12 and $1.17\,\mathrm{Hz}$). At station SLUW, the resonance frequency is therefore $1.15\,\mathrm{Hz}$.

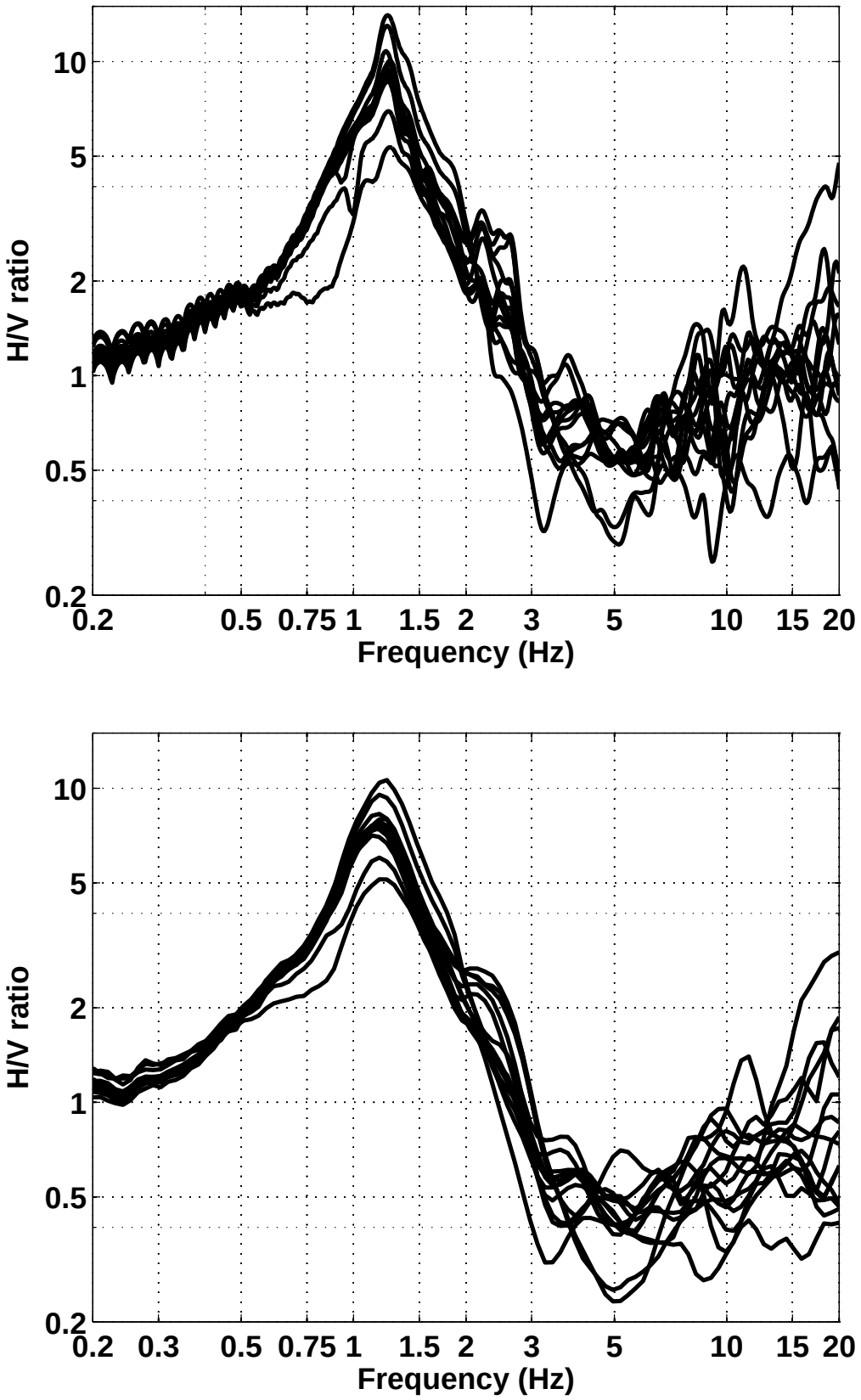

Figure 8: H/V spectral ratios using the standard method (Geopsy - top) and the TFA method (code V: Poggi - bottom).

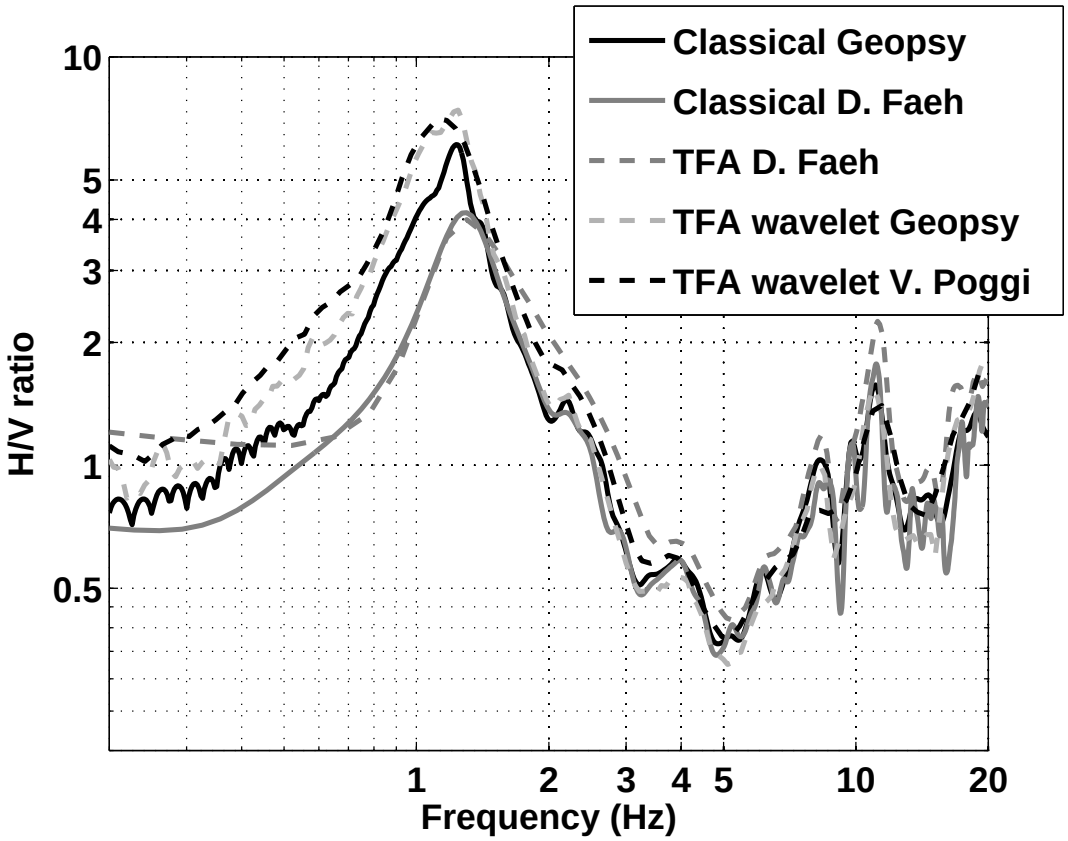

Figure 9: H/V spectral ratios using all available methods at point LUW000 (central point of the array). Classical methods were divided by $\sqrt{2}$.

4.3 Polarization analysis

Considering that SLUW is located in the deep glacial-lacustrine basin, a 2D or 3D resonance could occur. Therefore, polarization analysis on the array data was performed using the method of Burjánek et al. [2010]. All points (Fig. 10) show a weak polarization at 1.2 Hz in the direction of the main valley axis (NNW-SSE). It is likely to be related to 2D/3D resonance [Poggi et al., 2012c].

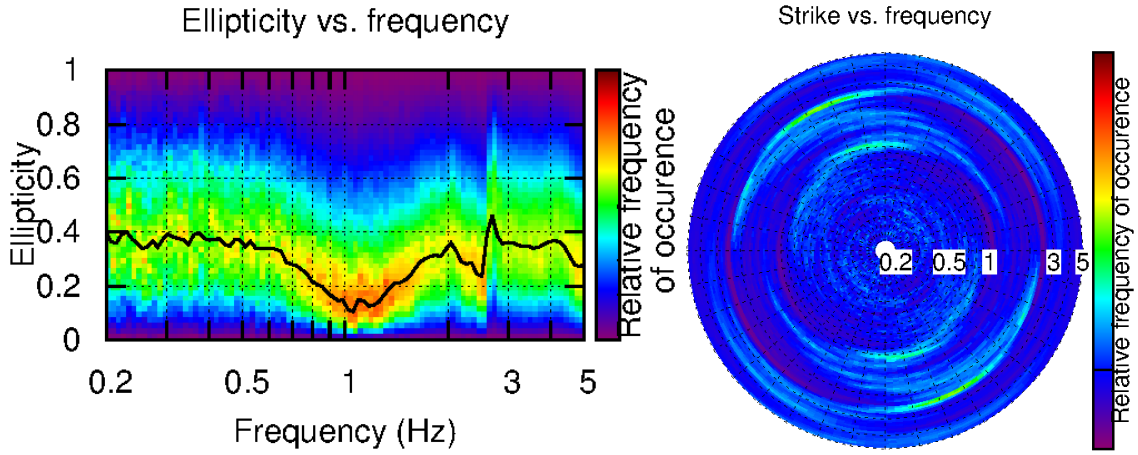

Figure 10: Polarization analysis at point LUW000. Left: Ellipticity (A trough in the ellipticity corresponds to polarized motion). Right: Strike of the polarization.

5 Processing

5.1 Processing methods and parameters for the passive data

The vertical components of the arrays were processed using the FK and the High-resolution FK analysis [Capon, 1969] using the Geopsy `http://www.geopsy.org` software. Large time windows were considered (500T) because it gave better results. All the consistent results were concatenated.

Moreover, a 3C array analysis [Fäh et al., 2008] was also performed using the array_tool_3D software [Poggi and Fäh, 2010] in order to derive Rayleigh and Love modes. The results of computations of both datasets were assembled to estimate the dispersion curves.

Method	Set	Freq. band	Win. length	Anti-trig.	Overlap	Grid step	Grid size	# max.
HRFK 1C	1	$0.8 - 15\,\mathrm{Hz}$	$500T$	No	50%	0.001	0.3	5
HRFK 3C	1	$2 - 10\,\mathrm{Hz}$	Wav. 10 Tap. 0.2	No	50%	100 m/s	1500 m/s	10

Table 5: Methods and parameters used for the array processing.

5.2 Processing methods and parameters of the active data

From the geophone recordings only the vertical direction is available for processing, while from the seismological stations both the vertical (channel 3) and the radial (channel 2, "North") directions of recording have been analyzed. In all cases the classical f-k approach and the t-f-k analysis [Poggi et al., 2012a] have been used, providing nevertheless comparable results. In this report, then, only the results from the second method are presented, which generally provides a less noisy representation of the higher modes. A tentative analysis of the transversal direction was also made, but the results have not been included in this report, since the employed sources do not give the possibility to directly generate anti-plane motion, and it is consequently not possible to rely on those results. Therefore, the following considerations are representative of Rayleigh-wave dispersion only.

5.3 Obtained dispersion curves from the passive analysis

The first mode (Rayleigh) in the 1C FK analysis could be picked between 2.6 and $7.4\,\mathrm{Hz}$ (Fig. 11). The velocities are low from $460\,\mathrm{m/s}$ at $2.6\,\mathrm{Hz}$ down to $130\,\mathrm{m/s}$ at $7.4\,\mathrm{Hz}$. Four different datasets were computed: using positioning done on the field only (1^{st} measurement), using positioning done on the field only (after the 2^{nd} measurement), using the post-processed GPS data and using only the 9 points that were accurately determined after the field work. Results are displayed on Fig. 11. The enhancement provided by more accurately located points is clear between the first and the second measurement: there is less scatter and the dispersion can be seen at much higher frequency. The low accuracy of points is destroying the dispersion data at high frequency. The post-processing (3^{rd} from the top) leads to slightly better results

compared to the unprocessed data. Using less but accurate points (bottom) gives much lower quality results, less broadband and with a higher standard deviation.

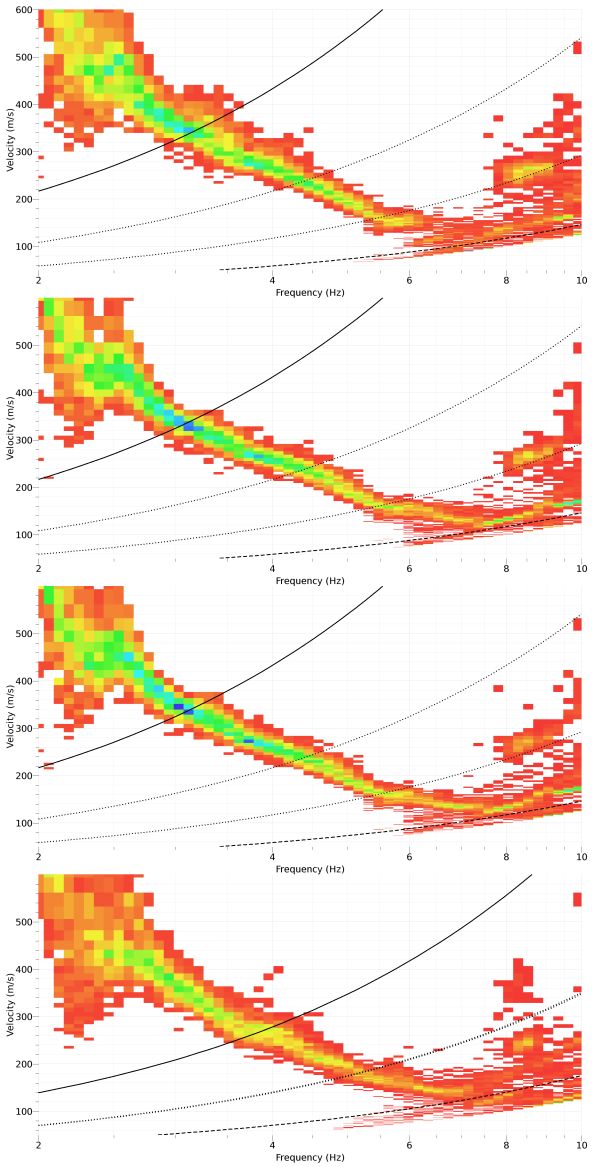

Figure 11: Comparison of the dispersion results using different datasets. From top to bottom: Positioning from the first GPS measurement, Positioning from both measurements, Positioning using the post-processing, Points with an accurate position from the field measurement only (9/14 points).

Using the 3C analysis, only fundamental Rayleigh mode can be picked (Fig. 12) from 2.7 to $6.3\,\mathrm{Hz}$. 1C and 3C analyses are in good agreement (Fig. 13). However, no dispersion can be seen neither on the radial nor on the transverse components.

Comparison with the SBB array, performed $200\,\mathrm{m}$ further NW is displayed in Fig. 14. It shows that they are in good agreement below $4\,\mathrm{Hz}$ but that the upper layer has a much lower velocity in SBB site.

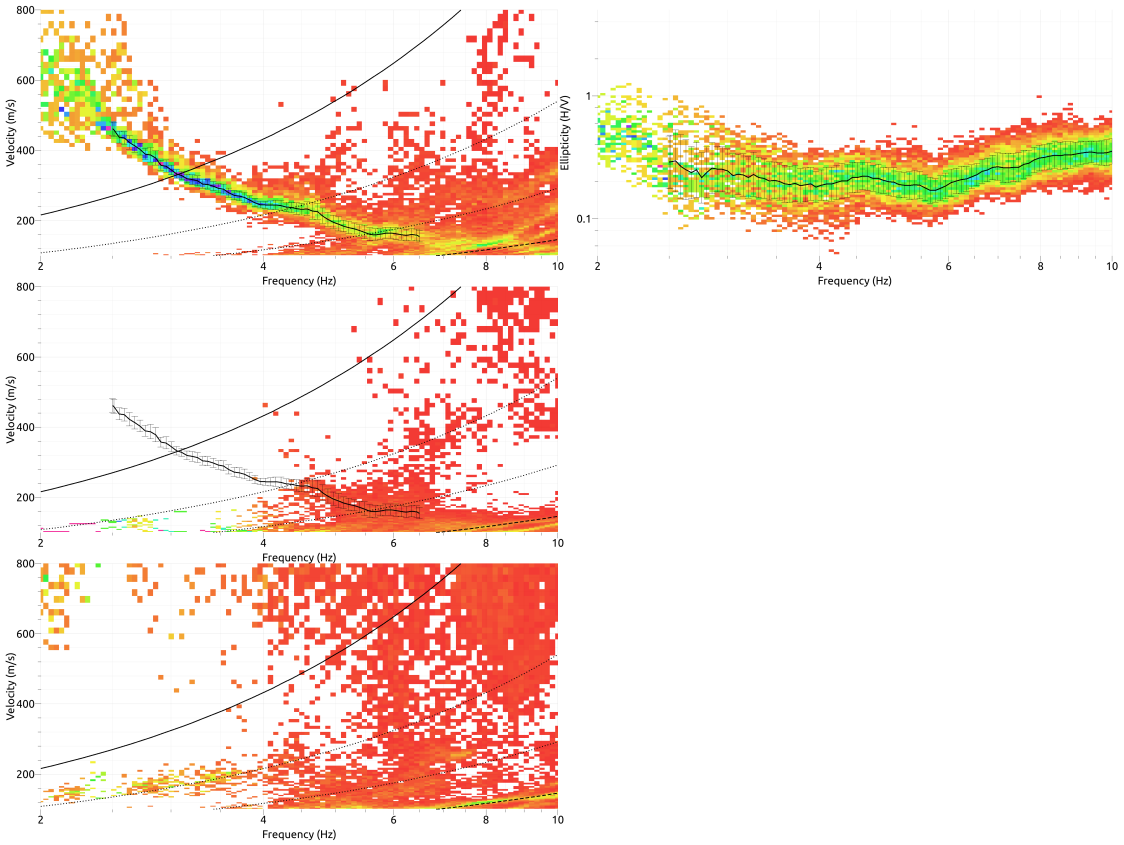

Figure 12: Histograms obtained from the 3C array analysis (from top to bottom: vertical, radial and transverse directions; on the right: ellipticity) and picking of the fundamental Rayleigh mode.

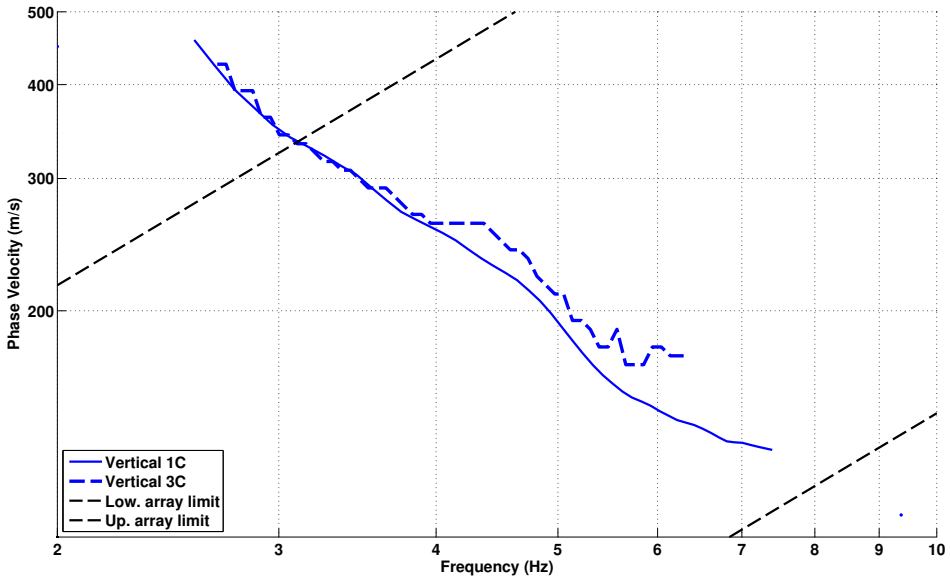

Figure 13: Comparison of obtained dispersion curves using 1C and 3C analyses for the Rayleigh mode.

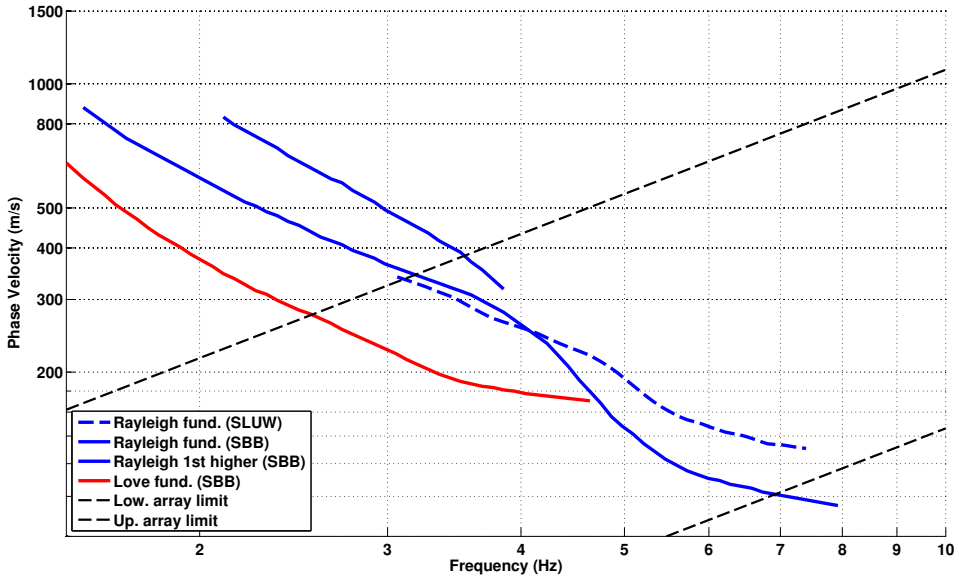

Figure 14: Comparison of obtained dispersion curves in LUW site and SBB site.

5.4 Obtained dispersion curves from the active analysis and merging with the passive results

By comparing the two shot offsets, better results were obtained using the lager distance (20m), especially for the generation of the higher modes. The results using the two equipments and for the vertical component of motion are mostly comparable (Fig. 15 and Fig. 16). Several surface wave modes are clearly identifiable in the velocity-frequency plane. The fundamental mode is stable at the velocity of about 120m/s, up to 15Hz; here a jump in the mode is present, which is however difficult to interpret at this stage; it can be either attributed to an external disturbance in the processing or to a feature of the modes (mode osculation and jump). Two different interpretations has been then proposed (Fig. 17). In the first, we propose an exchange of energy between the fundamental mode and the first higher at the osculation point. According to such interpretation, the fundamental mode is no more visible above 15Hz, as all the energy transfers to the above mode. In the second interpretation, on the contrary, the mode is considered unique till 40Hz, with just a weak velocity inversion. Unfortunately, we don't have any mean to propend for an interpretation or for the other at the present level of knowledge. Assessing the reliability of the two hypotheses can be nevertheless done a-posteriori, after analyzing the results of the inversion phase. On the other side, interpretation of the results from the processing of the radial component provided consistent results with the vertical, so that a unique model is finally provided.

Modes higher than the first one are probably too uncertain to be included in the analysis, as it can be deduced from the energy level in the f-k spectrum. Also the comparison between the Geode and Quanterra results shows a not always perfect matching of the second and the third higher mode. For this reason, these modes were then not included in the final inversion model.

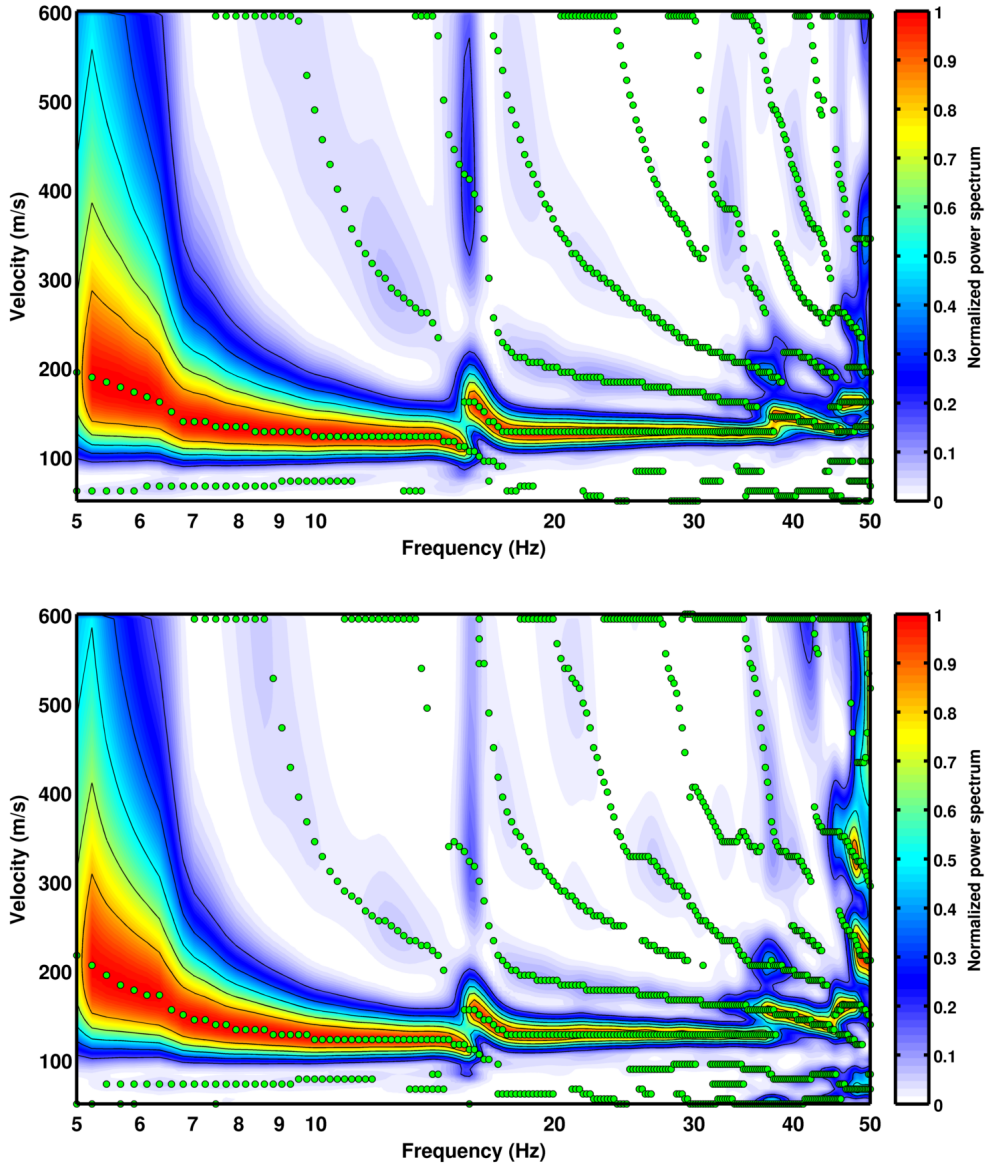

Figure 15: Results of processing the vertical direction using the geophone string (top) and the Lennartz sensors (bottom). In both cases, the analysis was performed with the wavelet t-f-k approach. Due to the different number of sensor employed (and therefore resolution) a progressive mismatching is visible for the high-modes above the third.

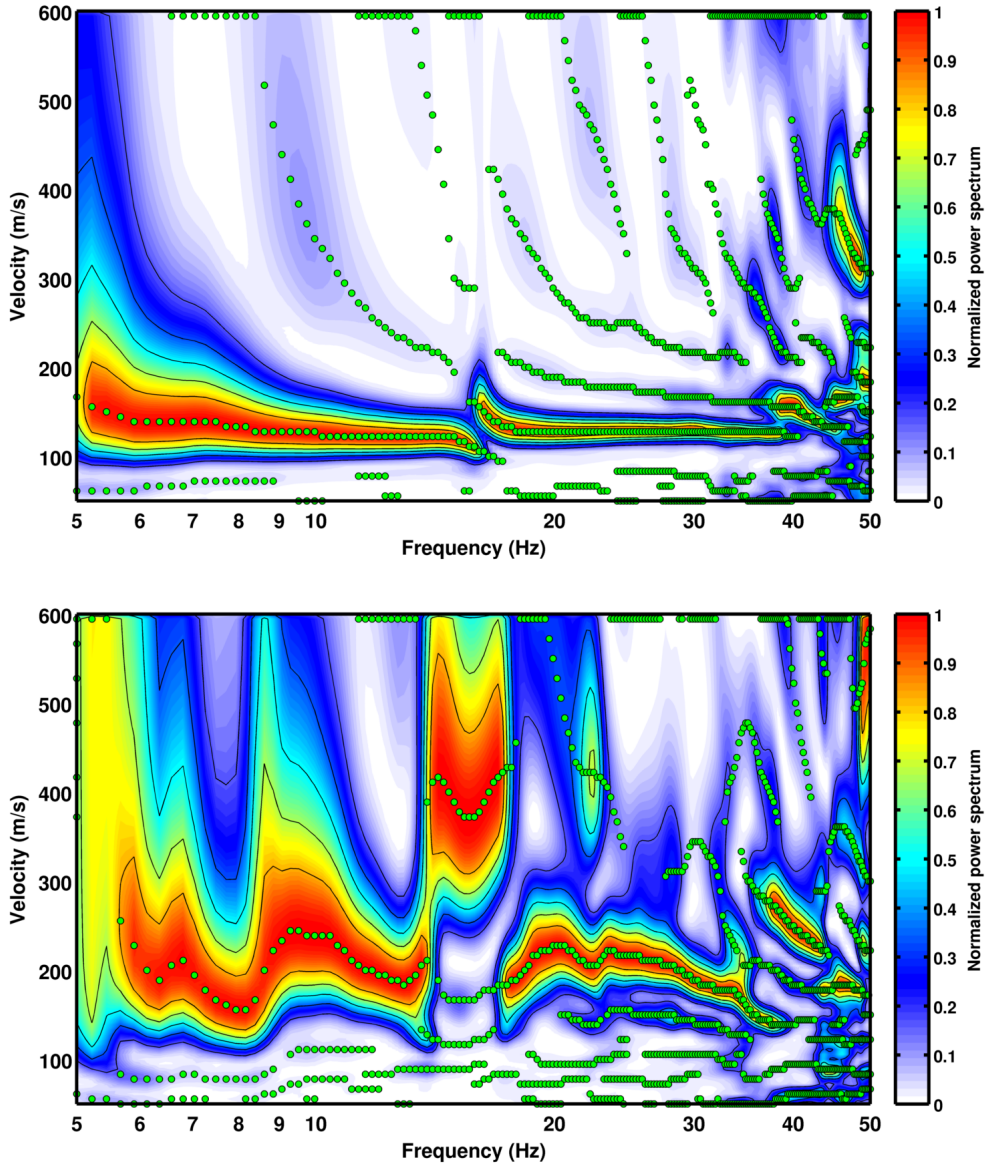

Figure 16: Results of processing the radial direction (top) and the transversal (bottom) using the Lennartz sensor array. This last was not used for the inversion.

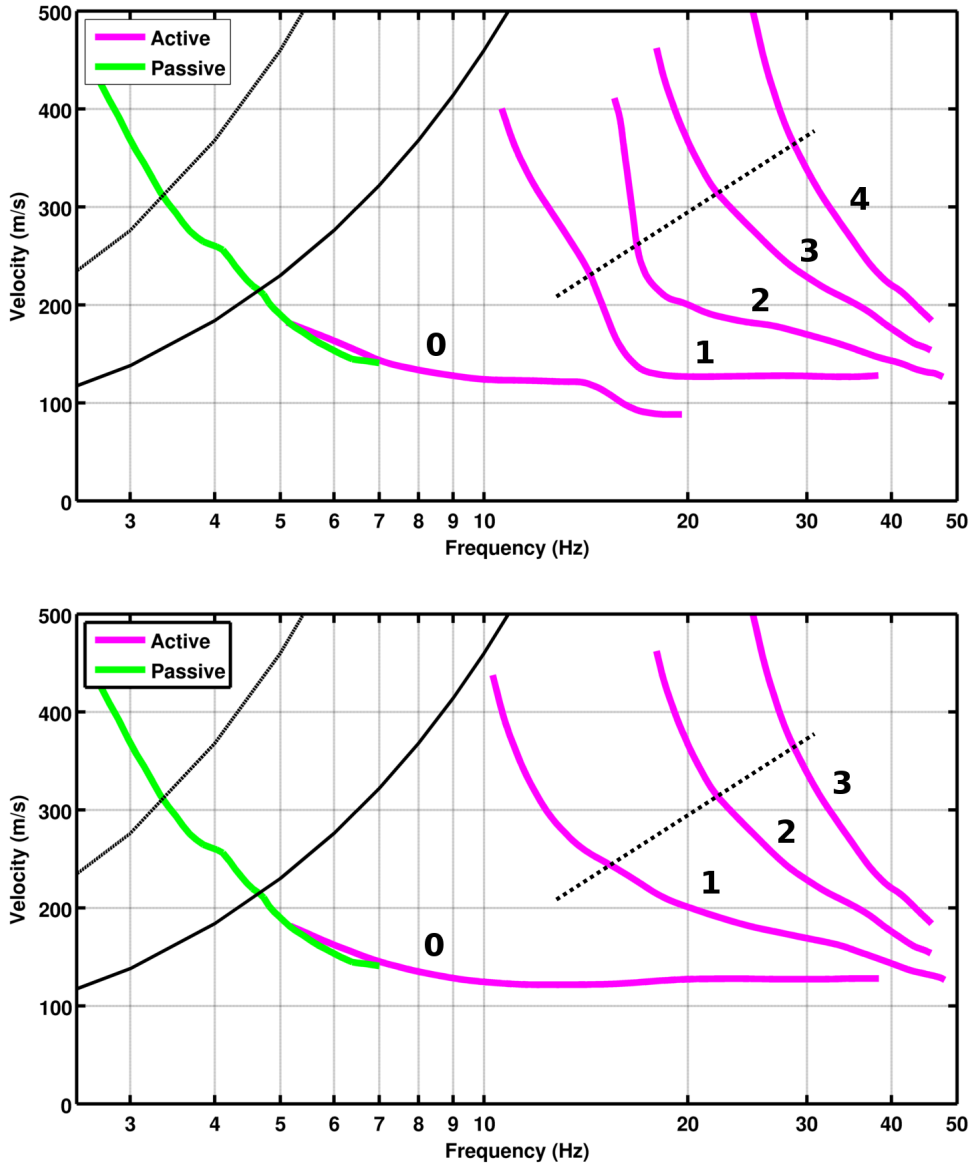

Figure 17: Comparison between the two interpretations of the modal dispersion pattern form the f-k spectrum in Fig. 15 (bottom). The fundamental mode is in good agreement with the result from a passive array survey performed on the same area The black dashed line indicates the limits over with the higher modes are not considered 100% reliable.

6 Results of the downhole experiment

The downhole experiment was processed by the Geoprofile company using an ad-hoc software. The picked signals are generated from the progressing of the probe into the ground and recorded at the surface. By picking the arrival times on the transverse component (Fig. 18), the downhole experiment allows to directly estimate the shear-wave velocities at each meter. It is not known how the company assumes the wave propagation from the source to the geophone (due to the offset). According to the company, the results on the first $5\,\mathrm{m}$ are not reliable.

Another picking is proposed here with a 4 layers interpretation (Fig. 19). The top part, however, might be questionable. The retrieved velocities are compared to the CPT measurement results on Fig. 20

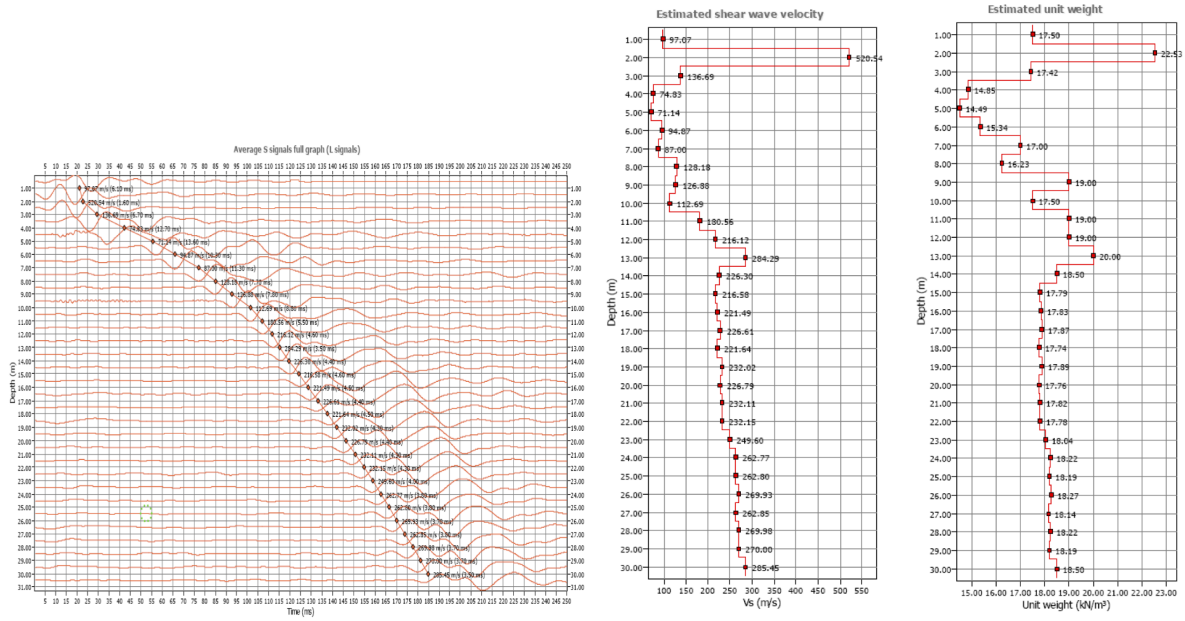

Figure 18: Recorded time histories from the downhole experiment (left) and interpretation in terms of shear wave velocity profile (right) from the company.

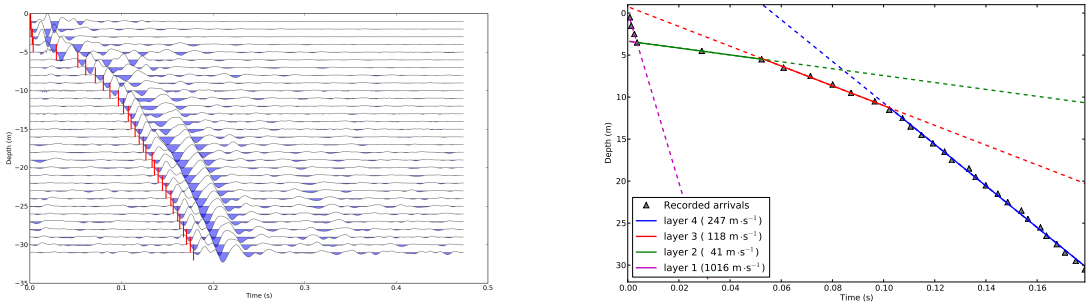

Figure 19: Recorded time histories from the downhole experiment (left) and interpretation in terms of shear wave velocity (right) from SED.

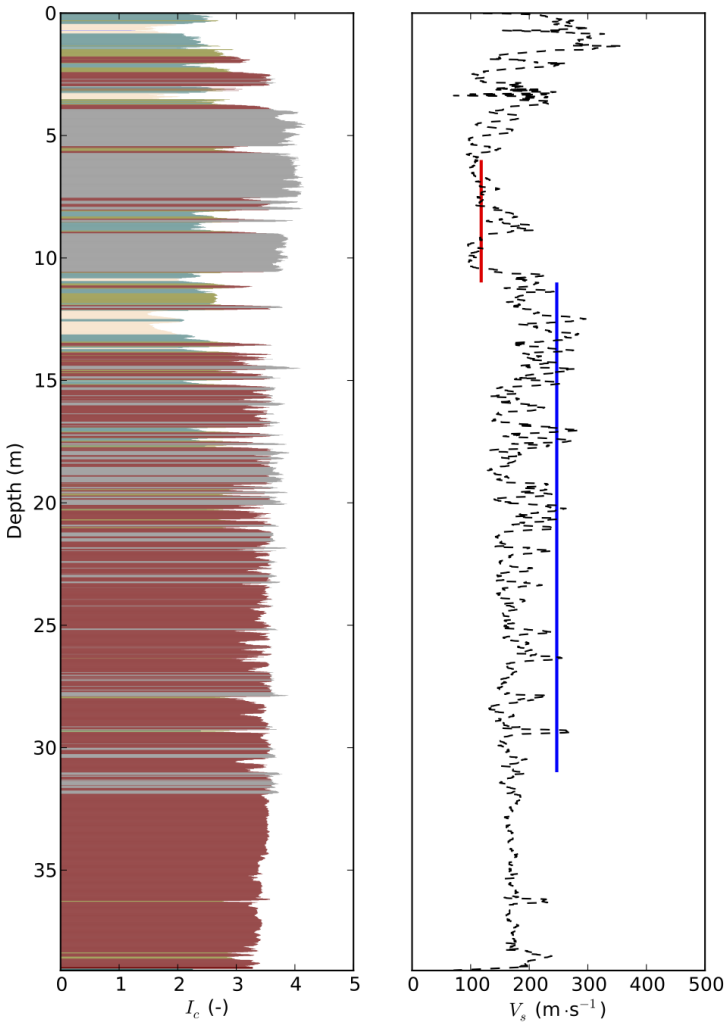

Figure 20: Comparison of the results from CPT measurement (on the left) and the related travel-time analysis (on the right) for the uppermost 40m of the soil profile of the station SLUW. A small velocity inversion is visible within the first 10m, which was then used as a priori for the following optimization procedure.

7 Inversion and interpretation

7.1 Inversion

For the inversion, a six-layer model was used. Search parameters were basically the layer thickness and the seismic velocities (P and S). These last were allowed to vary according to a range of Poisson's ratio between 0.1 and 0.4. Density was imposed to be constant (due to its little sensitivity to the phase velocity dispersion) at a value of about 2200Kg/m3 for the soft sediment part and 2800 for the bedrock. As already stressed, parameter search bounds were constrained using a-priori knowledge from a CPT and an ambient vibration survey performed in a nearby site [Poggi et al., 2012c].

Various inversion attempts were performed, using the different modal interpretations and data selections. As first the two interpretations from the active seismic survey were tested. The first interpretation required for a reasonable data fit the presence of a too strong velocity inversion in the uppermost layer. Please note that, although the use of velocity inversions improved the fitting of the data, this approach has to be used carefully, as it might lead to unstable and/or unrealistic solutions. Such model, moreover, is not supported by observation from downhole seismic analysis, and therefore this interpretation was rejected from any subsequent analysis. The second interpretation, conversely, provided consistent results. In this case, however, the inverted velocity model was capable to fully explain the fundamental and the first higher mode only.

To better resolve the deeper portion of the velocity model, the fundamental mode of the Rayleigh velocity dispersion curve have been extended at low frequency by adding the results from the passive acquisition survey (vertical component). This gave the possibility to extend the curve from 6Hz down to about 2.5Hz (Fig. 17). Complementary, to constraint on the bedrock interface below the sedimentary cover, which is ideally not resolved directly by the dispersion information, the Rayleigh wave ellipticity function has been analyzed by including the horizontal-to-vertical spectral ratio from single station recording of ambient vibration. The H/V curve was computed using the time-frequency wavelet approach proposed by Fäh et al. [2009]. At first, only a small portion of the Rayleigh ellipticity curve (the right flank, [Fäh et al., 2003]) was used, together the value of the site fundamental frequency (f0=1.1Hz). After some trials, it was possible to obtain a reliable data fit also for the left flank of the curve, adding useful information on the velocity contrast between sediment fill and bedrock.

7.2 Interpretation

The final velocity model (Fig. 22) consists in a low-velocity part with a small velocity inversion in the first 10 meters (Fig. 23 bottom), followed by a progressive increase below this depth, from about 300 to 1000m/s. The larger velocity contrast is found at about 200m (the bedrock interface), which is probably constrained by the use of the ellipticity information in the optimization. The bedrock velocity appears to be realistic (around 1800m/s), but should be confirmed from independent analysis. Overall the velocity model is consistent with a previous preliminary microzonation study of Lucerne [Poggi et al., 2012c], where a simplified modes consisting in a 10m low-velocity layer followed by a gradient was proposed.

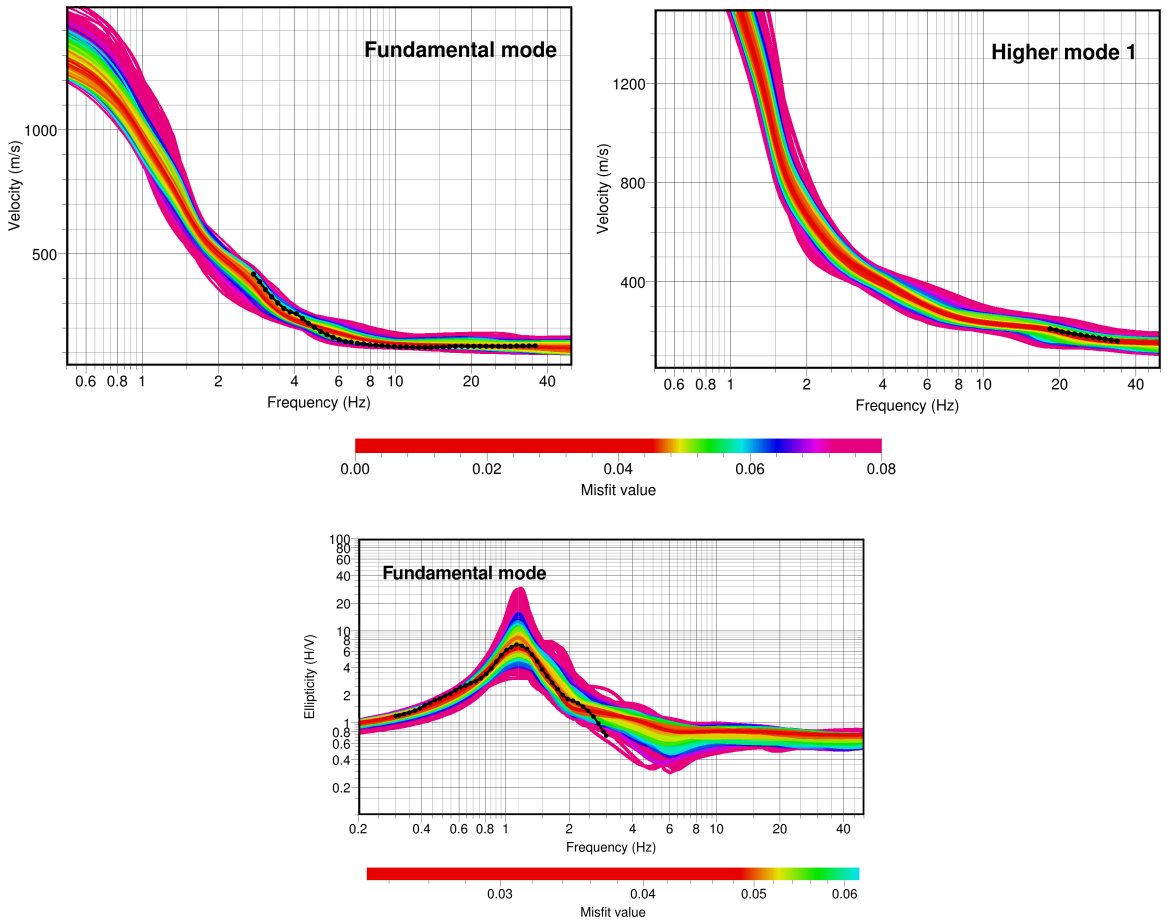

Figure 21: Top: Fit of all the dispersion curves generated during the inversion procedure, and sorted by increasing misfit. A reasonable fit is obtained for both the Rayleigh wave fundamental and first higher mode. Bottom: Fitting of the ellipticity function from single station time-frequency analysis of ambient vibrations. In this case both flanks show a reasonable match, as well as the resonance peak.

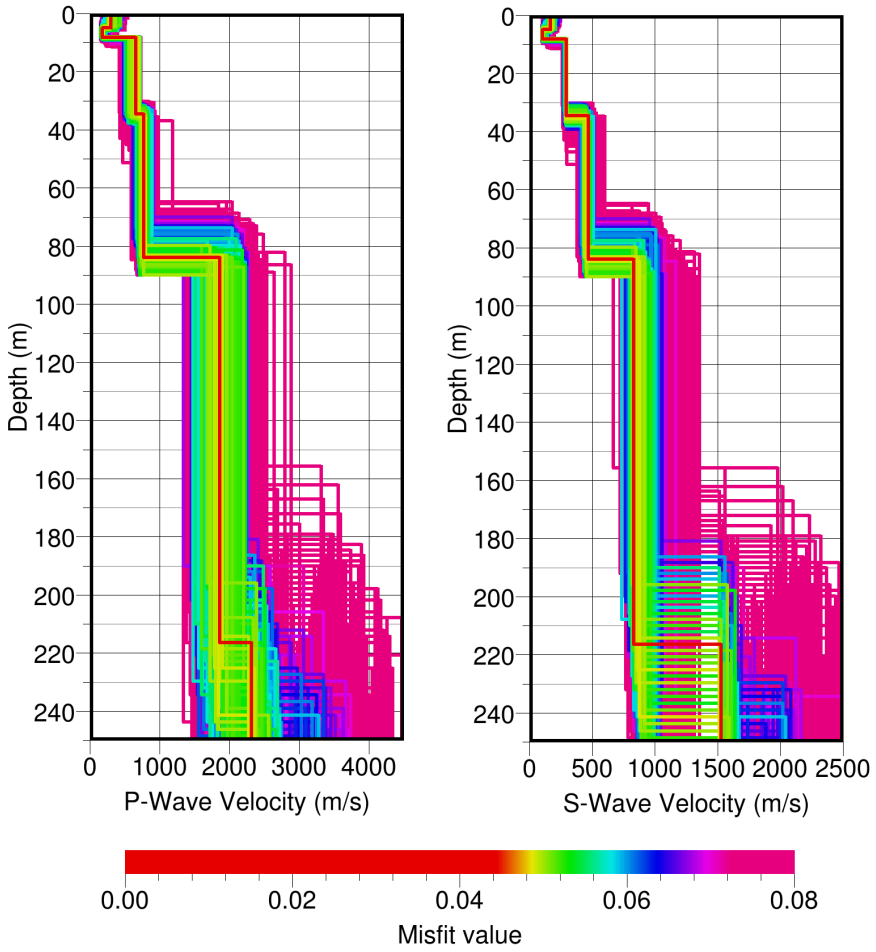

Figure 22: Ensemble of all the velocity profile modes (Vp on the left and Vs on the right) generated during the inversion (here the data from run 7) and sorted by increasing data misfit. Color-scale is compatible with that of Fig. 21.

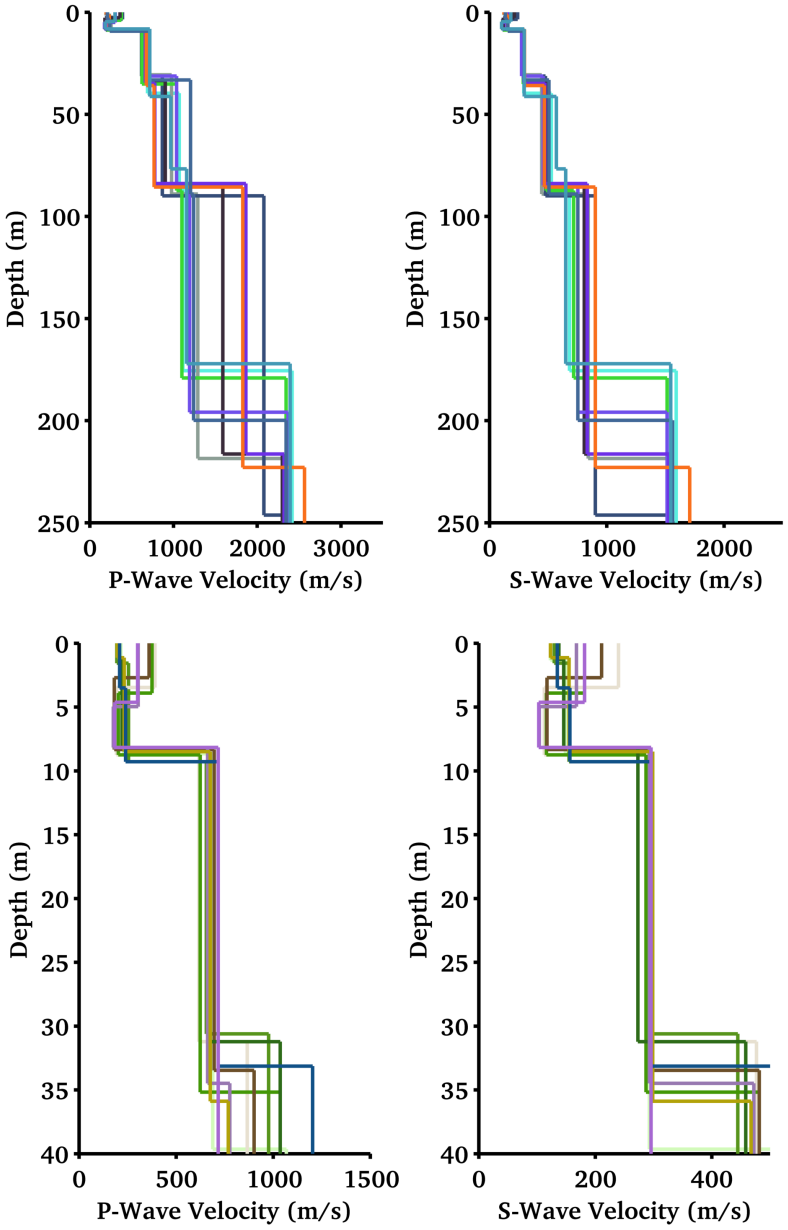

Figure 23: Top: Comparing the best fitting models of 10 different inversion runs (obtained using different initial seeds). These profiles are probably constrained down to 60 80m from the available dispersion curves (from active and passive). The bedrock at about 200m is complementary controlled by the ellipticity information. Bottom: Zoom of the first 40m of the models on the top figure.

7.3 Travel time average velocities and ground type

The distribution of the travel time average velocities at different depths was computed from the selected models. The uncertainty, computed as the standard deviation of the distribution of travel time average velocities for the considered models, is also provided, but its meaning is doubtful. $V_{s,30}$ is found to be $224\,\mathrm{m/s}$, which corresponds to class C in the Eurocode 8 [CEN, 2004] and D for SIA261 [SIA, 2003].

	Mean (m/s)	**Uncertainty (m/s)**
$V_{s,5}$	155	14
$V_{s,10}$	154	5
$V_{s,20}$	201	4
$V_{s,30}$	224	4
$V_{s,40}$	249	7
$V_{s,50}$	275	6
$V_{s,100}$	365	6
$V_{s,150}$	443	11
$V_{s,200}$	504	11

Table 6: Travel time averages at different depths from the inverted models. Uncertainty is given as one standard deviation from the selected profiles.

7.4 SH transfer function and quarter-wavelength velocity

The quarter-wavelength velocity approach [Joyner et al., 1981] provides, for a given frequency, the average velocity at a depth corresponding to 1/4 of the wavelength of interest. It is useful to identify the frequency limits of the experimental data (minimum frequency in dispersion curves at $2.5\,\mathrm{Hz}$ and the ellipticity peak at $1.15\,\mathrm{Hz}$ here). The results using this proxy show that the dispersion curves constrain the profiles down to $20\,\mathrm{m}$ and the ellipticity down to $70\,\mathrm{m}$ (Fig. 24). Moreover, the quarter wavelength impedance-contrast introduced by Poggi et al. [2012b] is also displayed in the figure. It corresponds to the ratio between two quarter-wavelength average velocities, respectively from the top and the bottom part of the velocity profile, at a given frequency [Poggi et al., 2012b]. It shows a trough (inverse shows a peak) at the resonance frequency.
Moreover, the theoretical SH-wave transfer function for vertical propagation [Roesset, 1970] is computed from the inverted profiles. It is compared to the quarter-wavelength amplification [Joyner et al., 1981] that however cannot take resonances into account (Fig. 25). In this case, the models are predicting large amplifications at the resonance peaks.

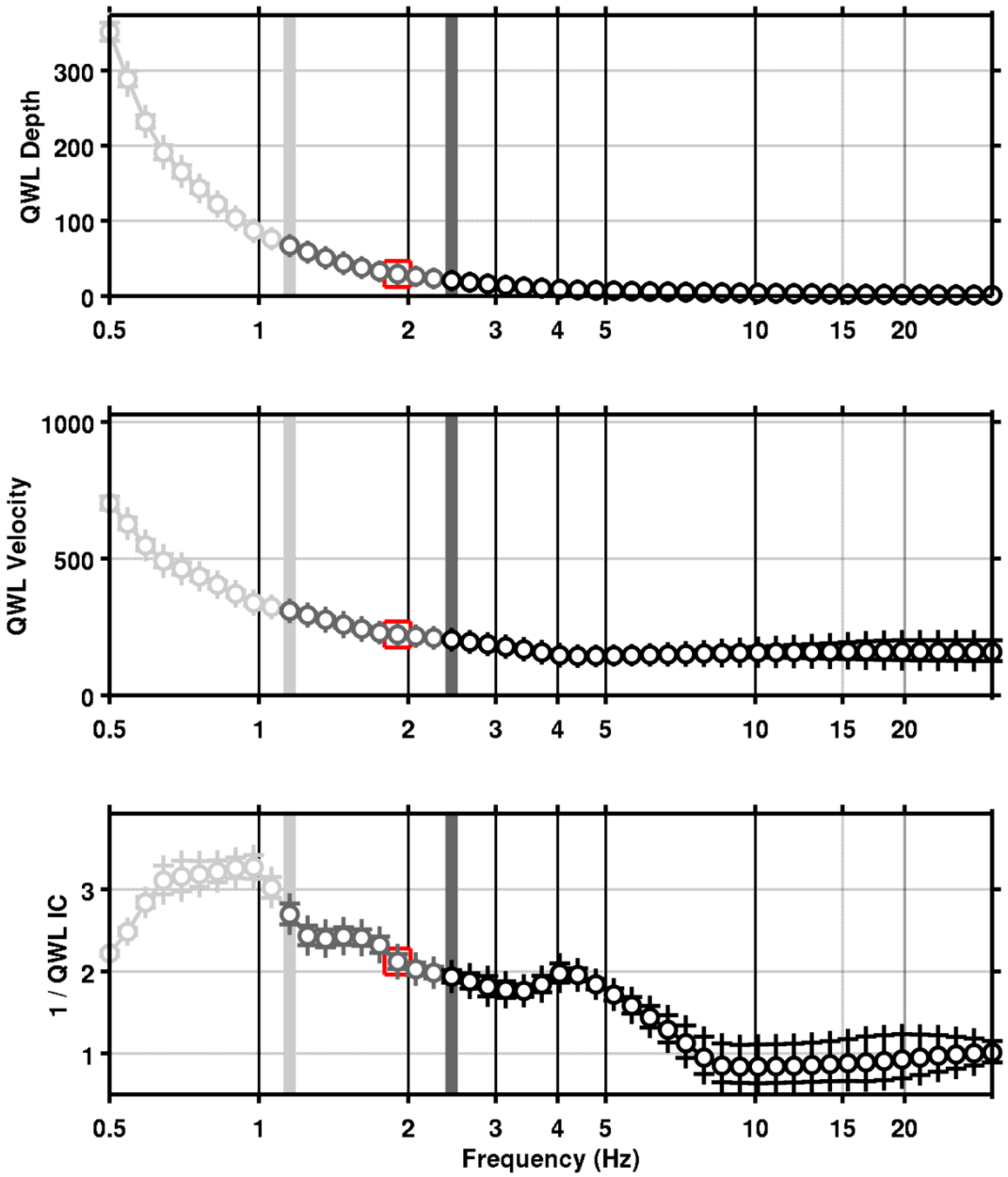

Figure 24: Quarter wavelength velocity representation of the velocity profile (top: depth, centre: velocity, bottom: inverse of the impedance contrast). Black curve is constrained by the dispersion curves, light grey is not constrained by the data. Red square is corresponding to $V_{s,30}$.

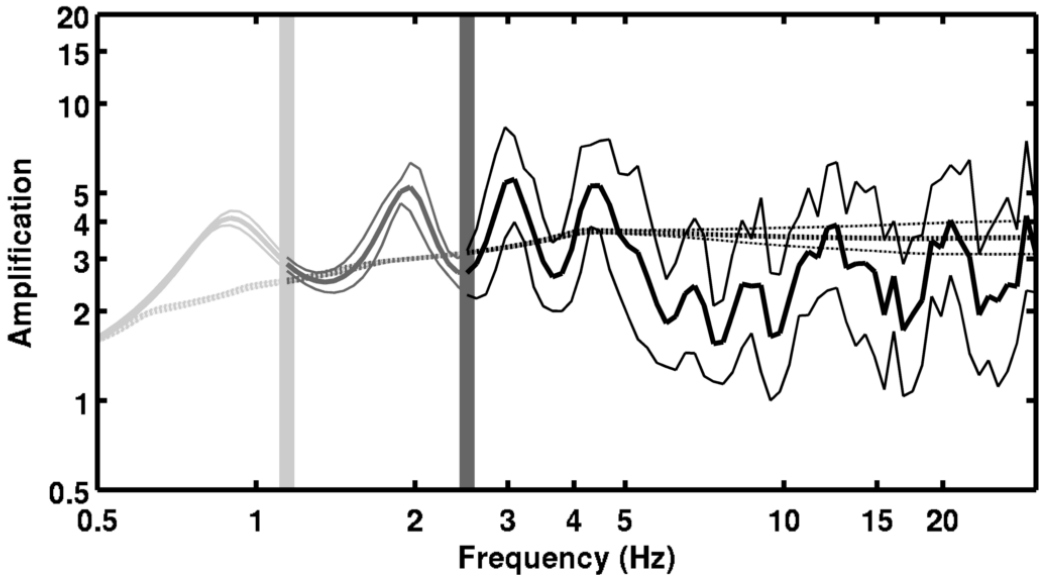

Figure 25: Theoretical SH transfer function (solid line) and quarter wavelength impedance contrast (dashed line) with their standard deviation. Significance of the greyshades is detailed in Fig. 24.

8 Conclusions

Combined analysis of passive and active seismics were used to derive a velocity model for the site of the SLUW station in Lucerne. The final velocity model consists in a low-velocity part with a small velocity inversion in the first 10 meters, followed by a progressive increase below this depth, from about 300 to 1000m/s. The larger velocity contrast is found at about 200m (the bedrock interface). The bedrock velocity appears to be realistic (around 1800m/s), but should be confirmed from independent analysis. A 3D behaviour of the sedimentary basin has been shown with a fundamental resonance peak at $1.15\,\mathrm{Hz}$. $V_{s,30}$ is $214\,\mathrm{m/s}$, which would correspond to ground type C in the Eurocode 8 [CEN, 2004] and D for the SIA261 [SIA, 2003]. The theoretical 1D SH transfer function and impedance contrast of the quarter-wavelength velocity computed from the inverted profiles show large amplifications at the resonance frequencies. Recordings on the new station will allow to compare to these simple models.

Acknowledgements

The author thanks Flavien Beaud for the help during the passive measurements, Armin Ziegler who provided the active source equipment and Benjamin Wallimann for the help during the active measurement.

References

Sylvette Bonnefoy-Claudet, Fabrice Cotton, and Pierre-Yves Bard. The nature of noise wavefield and its applications for site effects studies. *Earth-Science Reviews*, 79(3-4): 205–227, December 2006. ISSN 00128252. doi: 10.1016/j.earscirev.2006.07.004. URL http://linkinghub.elsevier.com/retrieve/pii/S0012825206001012.

Jan Burjánek, Gabriela Gassner-Stamm, Valerio Poggi, Jeffrey R. Moore, and Donat Fäh. Ambient vibration analysis of an unstable mountain slope. *Geophysical Journal International*, 180(2):820–828, February 2010. ISSN 0956540X. doi: 10.1111/j.1365-246X.2009.04451.x. URL http://doi.wiley.com/10.1111/j.1365-246X.2009.04451.x.

J. Capon. High-Resolution Frequency-Wavenumber Spectrum Analysis. *Proceedings of the IEEE*, 57(8):1408–1418, 1969.

CEN. *Eurocode 8: Design of structures for earthquake resistance - Part 1: General rules, seismic actions and rules for buildings*. European Committee for Standardization, en 1998-1: edition, 2004.

Donat Fäh, Fortunat Kind, and Domenico Giardini. A theoretical investigation of average H / V ratios. *Geophysical Journal International*, 145:535–549, 2001.

Donat Fäh, Fortunat Kind, and Domenico Giardini. Inversion of local S-wave velocity structures from average H/V ratios, and their use for the estimation of site-effects. *Journal of Seismology*, 7(4):449–467, October 2003. ISSN 1383-4649. doi: 10.1023/B:JOSE.0000005712.86058.42. URL http://link.springer.com/10.1023/B:JOSE.0000005712.86058.42.

Donat Fäh, Gabriela Stamm, and Hans-Balder Havenith. Analysis of three-component ambient vibration array measurements. *Geophysical Journal International*, 172(1):199–213, January 2008. ISSN 0956540X. doi: 10.1111/j.1365-246X.2007.03625.x. URL http://doi.wiley.com/10.1111/j.1365-246X.2007.03625.x.

Donat Fäh, Marc Wathelet, Miriam Kristekova, Hans-Balder Havenith, Brigitte Endrun, Gabriela Stamm, Valerio Poggi, Jan Burjanek, and Cécile Cornou. Using Ellipticity Information for Site Characterisation Using Ellipticity Information for Site Characterisation. Technical report, NERIES JRA4 Task B2, 2009.

William B. Joyner, Richard E. Warrick, and Thomas E. Fumal. The effect of Quaternary alluvium on strong ground motion in the Coyote Lake, California, earthquake of 1979. *Bulletin of the Seismological Society of America*, 71(4):1333–1349, 1981.

Katsuaki Konno and Tatsuo Ohmachi. Ground-Motion Characteristics Estimated from Spectral Ratio between Horizontal and Vertical Components of Microtremor. *Bulletin of the Seismological Society of America*, 88(1):228–241, 1998.

V. Poggi, D. Fäh, and D. Giardini. Time,ÄìFrequency,ÄìWavenumber Analysis of Surface Waves Using the Continuous Wavelet Transform. *Pure and Applied Geophysics*, 170(3): 319–335, June 2012a. ISSN 0033-4553. doi: 10.1007/s00024-012-0505-5. URL http://www.springerlink.com/index/10.1007/s00024-012-0505-5http://link.springer.com/10.1007/s00024-012-0505-5.

Valerio Poggi and Donat Fäh. Estimating Rayleigh wave particle motion from three-component array analysis of ambient vibrations. *Geophysical Journal International*, 180(1):251–267, January 2010. ISSN 0956540X. doi: 10.1111/j.1365-246X.2009.04402.x. URL http://doi.wiley.com/10.1111/j.1365-246X.2009.04402.x.

Valerio Poggi, Benjamin Edwards, and D. Fah. Characterizing the Vertical-to-Horizontal Ratio of Ground Motion at Soft-Sediment Sites. *Bulletin of the Seismological Society of America*, 102(6):2741–2756, December 2012b. ISSN 0037-1106. doi: 10.1785/0120120039. URL http://www.bssaonline.org/cgi/doi/10.1785/0120120039.

Valerio Poggi, Donat Fäh, Jan Burjanek, and Domenico Giardini. The use of Rayleigh-wave ellipticity for site-specific hazard assessment and microzonation: application to the city of Lucerne, Switzerland. *Geophysical Journal International*, 188(3):1154–1172, March 2012c. ISSN 0956540X. doi: 10.1111/j.1365-246X.2011.05305.x. URL http://doi.wiley.com/10.1111/j.1365-246X.2011.05305.x.

J.M. Roesset. Fundamentals of soil amplification. In R. J. Hansen, editor, *Seismic Design for Nuclear Power Plants*, pages 183–244. M.I.T. Press, Cambridge, Mass., 1970. ISBN 978-0-262-08041-5. URL http://mitpress.mit.edu/catalog/item/default.asp?ttype=2\&tid=5998.

SIA. *SIA 261 Actions sur les structures porteuses*. Société suisse des ingénieurs et des architectes, Zürich, sia 261:20 edition, 2003.